Thermoluminescence characteristics of BeO doped with Si, Mg, and Cr: Density functional theory calculations and One trap – One recombination center model simulations

E. Tsoutsoumanos [a,b,*], D. Tzeli [c,d], A. Avramopoulos [a], N. Laskaris [e], P.G. Konstantinidis [f], E. Travlou [c], N. Korakis [c], N.N. Lathiotakis [d], G. Kitis [f], G.S. Polymeris [b], T. Karakasidis [a]

[a] Condensed Matter Physics Laboratory, Physics Department, University of Thessaly, GR-35100, Lamia, Greece
[b] Institute of Nanoscience and Nanotechnology, NCSR "Demokritos", GR-15310, Ag. Paraskevi, Athens, Greece
[c] Laboratory of Physical Chemistry, Department of Chemistry, National and Kapodistrian University of Athens, GR-15771, Zografou, Athens, Greece
[d] Theoretical and Physical Chemistry Institute, National Hellenic Research Foundation, GR-11635, Athens, Greece
[e] Department of Industrial Design and Production Engineering, University of West Attica, GR-12244, Egaleo, Athens, Greece
[f] Nuclear and Elementary Particle Physics Laboratory, Physics Department, Aristotle University of Thessaloniki, GR-54214, Thessaloniki, Greece

ARTICLE INFO

ABSTRACT

The incorporation of first principles computational methods in Thermoluminescence (TL) enables the comprehensive investigation of the luminescent characteristics exhibited by solid materials. These calculations offer valuable insights into the electronic structures and thermal behavior, providing a deeper understanding of the underlying mechanisms. Density Functional Theory (DFT) is a powerful tool for predicting the electronic structure properties, as the Density of States (DOS) of materials. By theoretically depicting the electronic states arising from electron transitions, the present study focuses on the DFT study of undoped *BeO* and of *BeO* with substitutional Si^{4+}, Mg^{2+} and Cr^{3+}, Mg^{2+} doping, and the connection of TL emission caused by recombination of electrons in centers, as outlined in the One Trap – One Recombination (OTOR) center model. This approach offers essential details regarding the origins of electron traps, facilitating a deeper exploration of the intrinsic contribution of DFT in Stimulated Luminescence (SL) analysis.

1. Introduction

Thermoluminescence (TL) is a physical phenomenon in which certain insulating or semiconducting materials, when exposed to ionizing radiation or high-energy particles, absorb a fraction of this energy. When the material is subsequently heated or thermally stimulated, a fraction of the absorbed energy is re-emitted as photons in the visible spectrum [1]. This re-emission of light is used in materials science for dosimetry applications, as it provides information about the cumulative radiation exposure of the material. TL has been used in dosimetry since 1953 and finds a wide range of applications in nuclear, medical, and environmental sciences [2,3]. Such materials, commonly referred to as thermoluminescent dosimeters (TLDs), are utilized with

each TLD being suitable for specific dosimetric applications within certain dose region. Naturally, the distinctive characteristics of these TLDs may vary based on their structure, composition, or their size, and the specific environmental conditions to which they are subjected [4–6].

The present study emphasizes on a comprehensive examination of Beryllium oxide (*BeO*), mainly from a theoretical standpoint while delving into its composition, properties, and experimental TL characteristics. A significant portion of experimental literature [7–21] and a substantial number of works that explicitly delve into TL phenomena from a theoretical perspective [21–42] have extensively explored various stimulated luminescence (SL) phenomena in *BeO* and other preeminent TLDs, such as dose response [15,21], Optically Stimulated Luminescence (OSL) characteristics [8–14,17,18], dosimetric properties

[7,19,20], etc. Investigations of this kind form the basis for exploring a wide range of different physical approaches and exert a significant influence on experimental analysis. BeO is a commonly used TLD during the last two decades, even though it is an insulator, its thermal conductivity is higher than the one of many metals. This ensures a rapid and consistent heat transfer during the TL signal readout stage, resulting in a sensitivity comparable to other TLDs [42–44]. Secondly, its near-tissue equivalence ($Zeff = 7.14$) is very similar to those of biological tissues ($Zeff = 7.35 - 7.65$) and water ($Zeff = 7.51$), thus, it is ideal for medical dosimetry [42,45]. Moreover, it is insoluble in water, it is non-reactive with the majority of chemical agents, it is durable to mechanical forces, and can be formed into discs or rods at high temperature environment [44,45]. Despite being widely available and having a low price, its powder is extremely toxic [44–46].

The most widely used BeO dosimeter is Thermalox 995, manufactured by Materion Inc. It has a stable response after multiple uses and almost zero noise signals [44]. BeO Thermalox 995 (BeO_T) has a purity percentage of 99.5 % for the major phase and its main impurities include Si and Mg, while it also contains traces of Fe, Ca, Al, Cr and Ti [43,44]. BeO_T TL glow curve yields one main peak within the temperature region $100 - 250°C$ and another one at $\sim 350°C$ [44]. On the other hand, a more recent version of BeO dosimeter has been available commercially by the Turkish company Radkor (BeO_R). Aşlar et al. [47] showed that the composition of BeO_R is similar to BeO_T both in terms of structure and composition, with higher dopant concentration of Cr in BeO_R in comparison to the counterpart of BeO_T. However, experimentally, their main difference lies in their glow TL curves, where BeO_R has a double peak in the main dosimetric region [43,44].

The numerous advantages and characteristics of BeO TLDs have been a research topic for many studies. Their applications in *in-vivo* dosimetry have been recently studied in detail by Kara et al. [48] and by Santos et al. [49] since the response of the material was crucial for applications in medical dosimetry. Beryllium oxide has been doped with various elements such as B, N [50–52], Cu [53] and even Eu [54]. Moreover, many researchers focus on the comparison of BeO with other dosimeters such as Al_2O_3 and LiF [55,56]. Theoretically, the geometry and the electronic structure of C-doped BeO nanotubes [57] and N- or B- doped BeO monolayer have been investigated via Density Functional Theory (DFT). However, to our knowledge, the electronic structure of BeO doped with Mg, Si (Thermalox 995), and Mg, Cr (Radkor), specifically in relation to the investigation of their theoretical TL signal replication, has not been studied yet.

The current investigation aims at exploiting first principles calculations, and more precisely the combination of Density Functional Theory (DFT) calculations with simulations based on the well-established One Trap - One Recombination center (OTOR) model [31,37,38]. Considering the above, the present study pursues a fourfold objective: (a) to methodically reconstruct the crystalline structures of BeO_T and BeO_R by accounting for the unit cell dimensions analogous to impurities, thereby ensuring a realistic representation that accommodates actual conditions while being within the computational limitations; (b) to investigate the electronic structures of the examined cases by performing comprehensive calculations, including analyses of electronic band structures and density of states (DOS) across various configurations; (c) to use DFT calculations towards extracting as many parameters required to reconstruct each individual TL glow peak and thus to generate theoretical TL glow curves via the OTOR model for each material. These parameters/results obtained by DFT were integrated as initial simulation parameters for the OTOR simulations; finally (d) to ultimately compare the theoretically reconstructed TL glow curves to their experimental counterparts for both BeO-based dosimeters.

The present work aims to develop a theoretical framework that combines DFT and OTOR. This approach seeks to offer comprehensive insights into the intrinsic properties of any TLD material. By incorporating DFT calculations within the OTOR model, this methodology aims to enhance the predictive understanding of artificial materials beyond phenomenological and empirical observations.

2. Method of analysis

2.1. Density functional theory (DFT)

Density Functional Theory (DFT) was introduced by Hohenberg and Kohn (1964) [58,59], and is based on the assumption that all observables, for example the total energy, are functionals of the electron density. Through the Kohn-Sham construction [60] of an auxiliary single particle system, it became a mainstream and versatile theoretical framework. It is a very powerful tool for the calculation of the electronic structure of molecules and materials [58–60]. Within DFT framework, many different approximions known as exchange and correlation functionals are available today, suitable for diverse systems and properties.

In the case of materials with defects, i.e., the formation energy that is required in order to create a defect or an impurity X in charge state q, is defined as:

$$E^f[X^q] = E_{tot}[X^q] - E_{tot}[Material, bulk] - \sum_i n_i \mu_i + q[E_F + E_V + \Delta V] \qquad (1)$$

The total energy, denoted as $E_{tot}[X^q]$, is obtained through a supercell calculation in the presence of a single impurity or defect, X, within the cell. $E_{tot}[Material, bulk]$ is the total energy for the corresponding supercell containing only bulk material (in the present case BeO). Respectively, n_i indicates the number of host or impurity atoms of type i that have been introduced ($n_i > 0$) or eliminated ($n_i < 0$) from the supercell when that defect was created. μ_i denotes the corresponding chemical potentials of the material and represents the energy of the sources involved in the exchange of atoms. E_F is the Fermi energy level and E_V is the energy of the valence-band that expresses the formation energies of charged states. Lastly, according to the Makov–Payne approach, ΔV indicates the energy formation for a stable compound that serves as a corrective factor to align the reference potential to the defective supercell [27,28,61].

2.2. One trap – One recombination center (OTOR) model

The One Trap - One Recombination center (OTOR) model has been widely used to describe the thermoluminescence process in most materials. According to the model, each electron trap is associated to a single recombination center. When an electron becomes trapped in a defect, it can recombine with a hole after being thermally stimulated to the conduction band, releasing a photon detectable in a TL measurement. The initial phase in this simulation involves the irradiation stage, where electron transitions between traps are characterized by the following set of differential equations [29,31,62,63].

$$\frac{dT}{dt} = \beta \qquad (2)$$

$$\frac{dR}{dt} = X \qquad (3)$$

$$\frac{dn}{dt} = n_c \cdot A_n \cdot (N_1 - n) - n \cdot s \cdot e^{\left(-\frac{E}{k_B \cdot T}\right)} \qquad (4)$$

$$\frac{dm}{dt} = A_h \cdot n_v \cdot (M_1 - m) - m \cdot A_m \cdot n_c \qquad (5)$$

$$\frac{dn_c}{dt} = X - n_c \cdot A_n \cdot (N_1 - n) - m \cdot A_m \cdot n_c + n \cdot s \cdot e^{\left(-\frac{E}{k_B \cdot T}\right)} \qquad (6)$$

$$\frac{dn_v}{dt} = X - A_h \cdot n_v \cdot (M_1 - m) \qquad (7)$$

Where, $T(t) = T_0 + \beta \cdot t$ represents the heating function, in which $T_0 = 273\,K$, β is the heating rate $\left(\frac{K}{s}\right)$, X signifies the rate of formation of electron-hole pairs and the excitation dose, which is proportional to the dosage rate; the dose-rate will be $X = R(t)$, where t is the irradiation exposure measured in s. The time-depended variables $n_v(t)$ and $n_c(t)$, measured in units of cm^{-3}, represent the concentrations of free holes in the valence and the conduction band, respectively. $N_1\ (cm^{-3})$ represents the electron trap concentrations with instantaneous occupancies of $n(t)$, while $A_n\ (cm^3 s^{-1})$ is the trapping probability coefficient. $M_1\ (cm^{-3})$ denotes the concentration of recombination centers with instantaneous occupancy $m(t)$, the $A_h\ (cm^3 s^{-1})$ is the probability coefficient of holes in luminescence centers and $A_m\ (cm^3 s^{-1})$ is the electron recombination probability coefficient [29].

The relaxation stage is simulated by solving the same set of differential equations for an additional period after the excitation is switched off, specifically by setting $X = 0$. The relaxation stage lasted 10 s in all simulation processes. In the final simulation stage, the heating or stimulation stage, the following set of differential equations describes the transfer of electrons between traps [29,31,62,63]:

$$\frac{dn_i}{dt} = n_c \cdot A_n \cdot (N_i - n_i) - n_i \cdot s \cdot e^{\left(-\frac{E_i}{k_B \cdot T}\right)} \tag{8}$$

$$\frac{dn_c}{dt} = \sum_i \left\{ n_i \cdot s \cdot e^{\left(-\frac{E_i}{k_B \cdot T}\right)} - n_c \cdot A_n \cdot (N_i - n_i) \right\} + m \cdot A_m \cdot n_c \tag{9}$$

$$\frac{dm}{dt} = -A_m \cdot n_c \cdot m \tag{10}$$

Where, $N_i\ (cm^{-3})$ represent the electron trap concentrations of trap i with instantaneous occupancies of $n_i(t)$, in the present case when $i = 1$ then $n_1 = n$. The parameters $s\ (s^{-1})$ and $E_i\ (eV)$, represent the frequency factor, and the activation energy of the trap respectively ($E_1 = E$), while $k_B = 8.617 \cdot 10^{-5}\ (eV \cdot K^{-1})$ is the Boltzmann constant. For $i = 1, 2, 3, \ldots$, it describes an interactive system of multiple traps, whereas for $i = 0$, the system is considered as non-interactive [63].

2.3. The rationale behind the combination of DFT analysis and the simulations using the OTOR model

Each TL glow peak is characterized by the following parameters; the maximum intensity of the peak, I_m, the temperature corresponding to the maximum intensity, T_m ($°C$ or K), the activation energy E (eV), the kinetics order, b, the frequency factor, s (s^{-1}) and the total integrated intensity of the peak, being directly associated to the total trapped charge, n_0 [31].

In the framework of the present study, DFT provides the initial values for some among these aforementioned parameters; the theory can definitely provide values for both activation energy and the total integral, thus defining the value of the parameter I_m as well. The kinetics order parameter is directly related to the geometrical/symmetry features of the TL peak and thus to the FWHM, ω, making it hardly feasible to get initial value of the corresponding parameter using the DFT. The temperature of the maximum TL intensity, T_m it depends largely on the activation energy and to a lesser extent on the frequency factor, according to the standard TL theory. The case for the frequency factor is more complicated, as DFT cannot directly provide an initial value for it. Nevertheless, this quantity is correlated with the Debye frequency which can be implemented as the frequency factor, s [38]. In the present study, besides the value of the Debye frequency, the values from the corresponding literature will be also used.

Specifically, concerning the process flow, the DFT analysis is run initially. DFT-derived parameters, including trap energy levels and

concentrations, are extracted from the DOS plots and fed into the OTOR model for TL simulations. These values were used as inputs, where the initial electron trap concentration and activation energies were calibrated based on DFT outputs. More precisely, the trap depth was determined by identifying energy states below the conduction band, and the trap occupancy was normalized based on the electron densities. First-order kinetics were assumed for all cases unless otherwise indicated by the comparison with experimental data.

2.4. Computational details

All electronic and structural calculations were performed using the QUANTUM ESPRESSO (QE) software [64], an implementation of DFT for periodic systems which is based on plane waves expansion of the orbitals and pseudopotentials. It is a popular used code for materials modeling at the nanoscale, applying periodic conditions. The total energy, electronic, and structural properties were obtained out utilizing the Perdew-Burke-Ernzerfhof (PBE) exchange-correlation functional within the Generalized-Gradient-Approximation (GGA) framework [65]. For the present study, the implemented valence electronic configurations in the pseudopotentials are: [Be: $1s^2\ 2s^2$], [O: $1s^2\ 2s^2\ 2p^4$], [Si: $1s^2\ 2s^2\ 2p^6\ 3s^2\ 3p^2$], [Cr: $1s^2\ 2s^2\ 2p^6\ 3s^2\ 3p^6\ 3d^3$], and [Mg: $1s^2\ 2s^2\ 2p^6\ 3s^2$]. Following the acquisition of DFT results, numerical integration of the One Trap-One Recombination center (OTOR) model was conducted in Python, specifically using the *scipy.integrate.odeint*. This process aimed to simulate the interaction between ionizing radiation and various crystal arrangements for each specific case.

2.4.1. Self-consistent field (SCF) calculations

Based on the Hohenberg-Kohn (HK) theorems and Kohn-Sham (KS) equations, the electron density for a system of N electrons is defined as the following multiple integral:

$$\rho(\vec{r}) = N \int \ldots \int |\Psi(\vec{\chi_1}, \vec{\chi_2} \ldots \vec{\chi_N})|^2 ds_1 d\vec{x_1} \ldots d\vec{x_N} \tag{11}$$

Where, N is the number of electrons, and $\Psi(\vec{\chi_1}, \vec{\chi_2} \ldots \vec{\chi_N})$ denotes the wave function of the system. The probability of finding any of the N electrons, within the volume element $d\vec{r_1}$ of arbitrary spin, is given by the integral over all spin coordinates and one spatial variable [66].

The HK theorem asserts that the ground-state energy is a functional of the electron density and is minimized only when this function accurately represents the true ground state of the system [59,66]. In the KS formalism, the system of interacting electrons is replaced by an auxiliary system of non-interacting electrons subject to an effective potential, the Kohn-Sham potential. The auxiliary KS system is defined to reproduce the same electron density as the system of interacting electrons. KS potential has a term known as exchange and correlation that needs to be approximated. It is a functional of the density, thus, KS equations have to be solved self-consistently. The kinetic energy is defined as:

$$T = -\frac{1}{2} \sum_i^N \langle \Phi_i | \nabla^2 | \Phi_i \rangle \tag{12}$$

T differs from the actual kinetic energy of the system. To address this disparity, the residuals of the true kinetic energy are incorporated as exchange-correlation energy. The energy expression for this system can be described as the sum of kinetic energy and the energy arising from the interaction with the external potential [60,66].

Self-Consistent Field (SCF) employs an iterative method, commencing by arbitrarily selecting an electron density function. Subsequently, the KS Equations are solved based on this function, yielding a set of orbitals utilized to derive a new electron density function. The process involves a convergence check, where the new electron density function is compared to the previous one. If the difference falls within the desired scale, the calculation proceeds to determine the total energy

of the system and other properties using the converged density function [66].

2.4.2. Supercell size and optimization

To model the simultaneous presence of various point defects resulting from either doping or the interaction of ionizing radiation with the crystal, an initial system was created by considering a multiple *BeO* unit (primitive) cells, known as a supercell. The selection of the optimum supercell size was made based on the maximization of the capacity for simulating point defects simultaneously. To fully comprehend the impact of each point defect on the electronic properties of the host material, it was essential to identify the minimum interaction between two defects.

The Crystallographic Information File (CIF) was downloaded from the Materials Research project, an open-access database [67].

Three different structures were examined, each with varying dimensions.

1. A structure with dimensions $3 \times 3 \times 1$, consisting of 27 *Be* and 18 *O* atoms. The substitution of one *Be* atom corresponds to an approximate doping percentage of 3.7%.
2. A structure with dimensions $3 \times 3 \times 2$, containing 45 *Be* and 36 *O* atoms. Substituting one *Be* atom in this case results in an approximately 2.2% doping percentage.
3. A structure with dimensions $3 \times 3 \times 3$, composed of 63 *Be* and 54 *O* atoms. Substituting one *Be* atom in this structure leads to an approximate doping percentage of 1.6%.

A $3 \times 3 \times 1$ structure provides a balanced doping percentage and computational efficiency, staying below the 10% threshold, which is deemed satisfactory. Additionally, for a second substitution (*Mg*), the doping percentage approaches 7.4%, still below the 10% limit. Experimental studies in artificial dosimeters have demonstrated doping percentages higher than 10% [17,43,44]. For structure optimization, the primary significance lies in determining the most stable and energetically favorable arrangement of atoms in a given system. The primary focus of this study centers on the substitution of a native *Be* atom with a foreign one, specifically *Si*, *Cr*, or *Mg*, within the compact structures of *BeO*. Through a meticulous examination of several different placements, it was observed that the results did not exhibit significant differentiation based on the specific location of the foreign atom within the crystal structure. The $3 \times 3 \times 1$ solid supercells structures of *BeO* and the ones doped with *Cr* and *Si* as well as with both *Cr*, *Mg*, and *Si*, *Mg* were
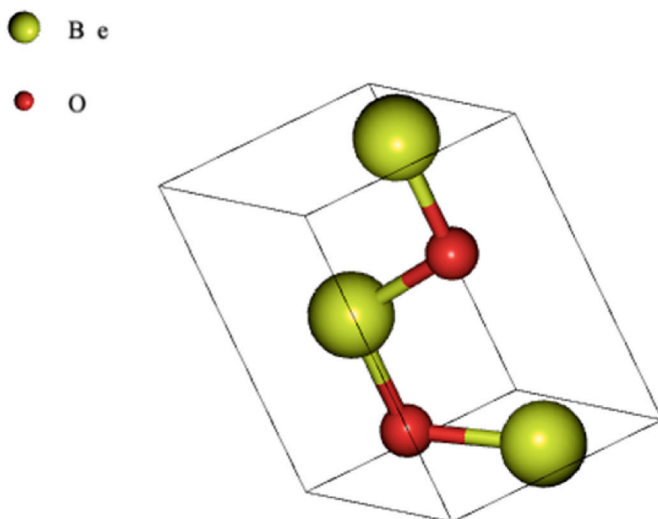
Fig. 1. BeO primitive cell (mp-2542, https://doi.org/10.17188/1200608), which contains 3 Be and 2 O atoms.

obtained by modelling in each case a different substitutional position (Fig. 1 and 2) (see Fig. 3).

The calculations were carried out by alternating the *Si*, *Cr* and *Mg* (substitutional atoms/dopants) between two equivalent positions for each structure. As previously mentioned, the DFT methodology based on the generalized gradient approximation (GGA) with the Perdew–Burke–Ernzerhof (PBE) functional to describe the electron exchange and correlation in order to minimize their energy [65]. The PBE pseudopotentials of QE, i.e., Be.pbe-rrkjus.UPF, O.pbe-rrkjus.UPF, Si.pbe-rrkj.UPF, Cr.pbe-sp-van.UPF, Mg.pbe-spnl-rrkjus_psl.1.0.0.UPF, were used [68], while taking into account the effect of long-range interactions that were added according to the DFT-D3 [69] dispersion corrected functional. The kinetic energy cut-off was set to 25 *Ry*, the SCF convergence threshold to 10^{-6} and the residual forces criteria to 10^{-3}. For the reciprocal space sampling, a $10 \times 10 \times 5 \times 0 \times 0 \times 0$ Monkhorst-Pack mesh was used for all calculations.

2.5. Validation of the simulation results

The validation of the initial conditions has been assessed through classical TL analysis methods such as Computerized Glow Curve Deconvolution (CGCD) method [70–73] and Peak Shape method (PSM) [74–77]. In PSM, by defining the quantities $\delta = T_2 - T_m$, $\tau = T_m - T_1$, $\omega = T_2 - T_1$ and $\mu_g = \delta/\omega$, the derivations of the mathematical expressions are given in form:

$$C_\omega = \frac{\omega \cdot I_m}{\beta \cdot n_0} \tag{13}$$

$$C_\delta = \frac{\delta \cdot I_m}{\beta \cdot n_m} \tag{14}$$

$$C_\tau = \frac{\tau \cdot I_m}{\beta \cdot (n_0 - n_m)} \tag{15}$$

Where, I_m expresses the maximum intensity of the TL peak, β is the heating rate, $n_m = \int_{T_m}^{\infty} I \, dt$ is the concentration of trapped electrons at maximum (half integral at high temperature maximum) cm^{-3}, $n_0 = \int_0^{T_{max}} I \, dt$ is the initial concentration of trapped electrons (total integral) cm^{-3} and $C_\omega, C_\delta, C_\tau$ are the quantities that characterizing the degree by which the area of a single glow peak approaches the area of a triangle [74–77].

The estimation of kinetic order is based on ω and the integral symmetry factor (or characteristics factor), defined as the ratio of the concentration of trapped electrons at maximum (n_m) over the initial concentration of trapped electrons (n_0), thus $\mu'_g = \frac{n_m}{n_0}$. The kinetic order of a TL glow-peak is determined using an iteration method [76] by the following mathematical expression:

$$\mu'_g = \left[\frac{b}{1 + (b-1) \cdot \Delta_m} \right]^{\frac{1}{1-b}} \tag{16}$$

Where, $\Delta_m = 2 \cdot k_B \cdot T_m / E_\alpha$; the activation energy parameter (E_α) was determined based on the initial conditions and it was set according to DFT calculations. The parameter T_m corresponds to the temperature at which the maximum TL intensity (I_m) occurs.

The activation energy, denoted as E_a, has been estimated through the following expression:

$$E_a = C_\omega \cdot \left(\frac{b}{b^{b-1}} \right) \cdot \frac{k_B \cdot T_m^2}{\omega} - 2 \cdot k_B \cdot T_m \tag{17}$$

Concerning the validation of theoretical results via CGCD, as described by Konstantinidis et al. (2021) and Kitis and Pagonis (2023) [34,73], the mathematical expressions are deriving by utilizing the Lambert-W function. In the present study, the validation of this premise was investigated through the following expressions [71]:
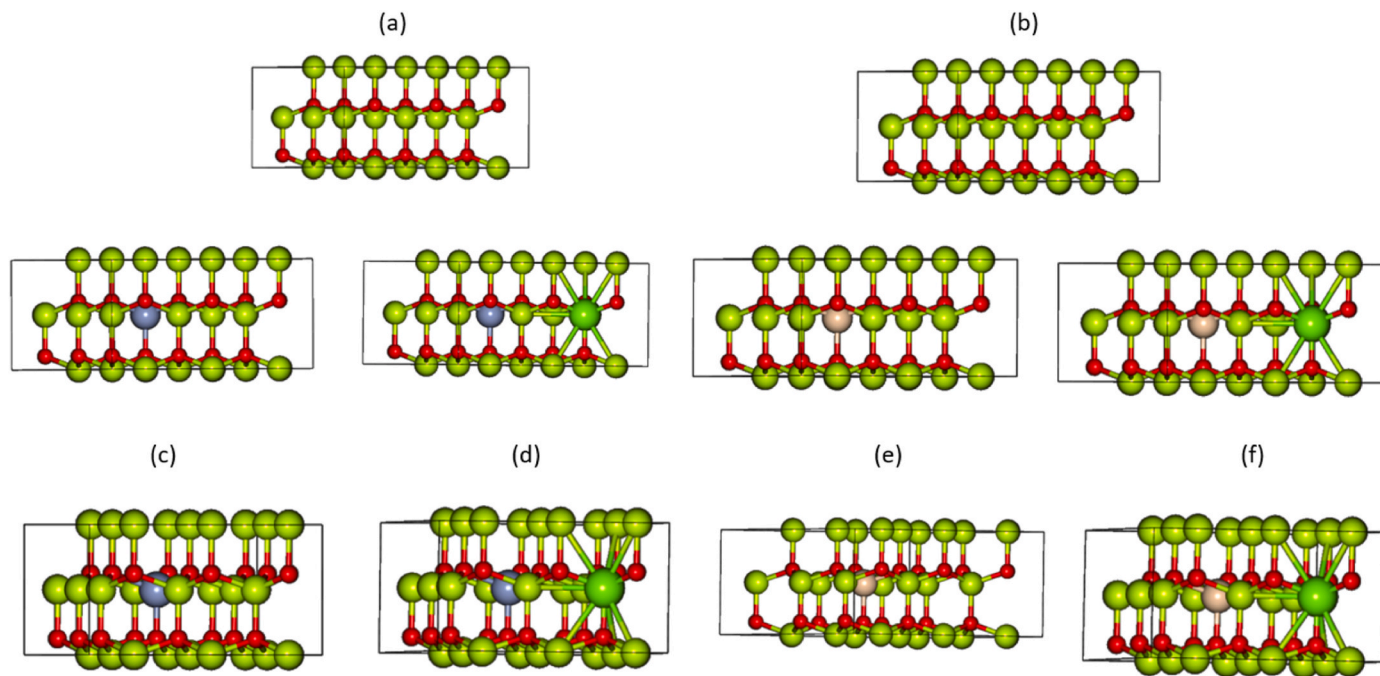
Fig. 2. Crystal structures and arrangements of each studied case. Beryllium is depicted in light green, Oxygen in red, Chromium in blue, Magnesium in dark green and Silicon in pink. Cells (a) and (b) show the BeO undoped structure, cell (c) presents the BeO doped with Cr while (d) corresponds to BeO doped with both Cr and Mg, corresponding to the Radkor BeO structure. Similarly, cell (e) presents BeO doped with Si and (f) the BeO doped with Si and Mg, which corresponds to the BeO Thermalox structure.
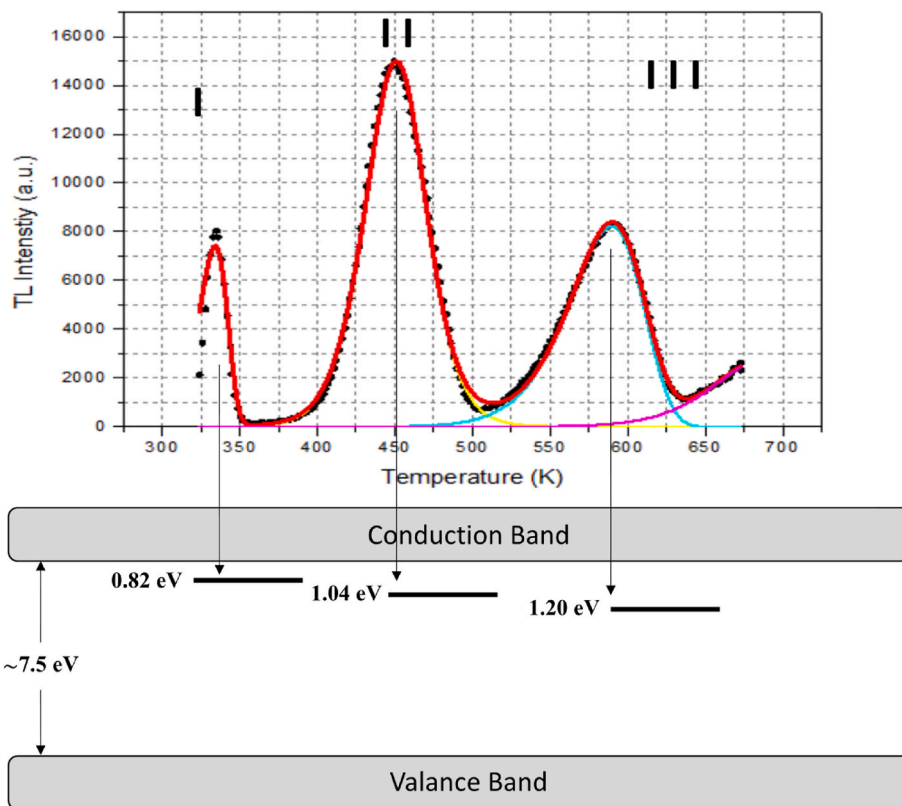
Fig. 3. A deconvolved experimental TL signal of BeO Thermalox 995 using CGCD. In this graph each TL peak (I, II, III) corresponds to an energy trap state below the Conduction Band.

$$I = I_m \exp\left(\frac{E\cdot(T - T_m)}{k_B\cdot T\cdot T_m}\right) \frac{W[e^{z_m}] + W[e^{z_m}]^2}{W[e^z] + W[e^z]^2} \tag{18}$$

$$z = \frac{R}{1 - R} - \ln\left(\frac{1 - R}{R}\right) + \frac{Ee^{\frac{E}{k_B\cdot T_m}}}{k_B\cdot T_m^2} \frac{F(T, E)}{1 - 1.05\cdot R^{1.26}} \tag{19}$$

$$F(T, E) = T\cdot e^{-\frac{E}{k_B\cdot T}} + \frac{E}{k_B}\cdot Ei\left(-\frac{E}{k_B\cdot T}\right) \tag{20}$$

Where $T(t) = t + T_0$ represents the temperature value at each time point, and t is a specific point in time, $T_0 = 273\,K$, I_m (a. u.) is the maximum TL intensity, R is the re-trapping ratio, and $Ei(x) = \int_{-\infty}^{x} \frac{e^t}{t} dt$ stands for the exponential integral function.

The quality of fit was assessed by evaluating the goodness of fit through the optimization of the four free fitting parameters (I_m, T_m, E_a, R), as well as the figure of merit (FOM). The FOM is defined as:

$$FOM = \frac{\sum \left|y_i^0 - y_i^f\right|}{\sum \left|y_i^f\right|} \tag{21}$$

This function is commonly applied in cases of CGCD deconvolution analysis, as described by Horowitz and Yossian (1995) [78]. In this function y_i^0 corresponds to the simulated data points, while y_i^f represents the theoretical data points deriving by alterations of the free parameters.

In the validation process, both deconvolution analysis and PSM were employed to cross-check and validate the simulation results. CGCD decomposes the experimental TL glow curve into individual TL peaks and adjusts kinetic parameters using non-linear fitting algorithms to achieve the best match with the theoretical model, with the goodness of fit assessed through statistical criteria, the figure of merit. PSM, in contrast, relies on the geometric properties of the glow peaks, such as FWHM and peak temperature, to estimate kinetic parameters through an analytical and geometrical approach. Parameters obtained from deconvolution process were cross-checked against those from PSM, ensuring consistent and accurate resolution of overlapping peaks and a robust TL glow curve analysis.

2.6. Electronic band Structure and density of states

The electronic band structure and density of states (DOS) are crucial for understanding the properties of materials. The electronic band structure provides information on the reciprocal-space dependence of the energy levels, while the DOS gives the distribution of electronic states with respect to their energy. In TL, the accurate depiction becomes pivotal, as it enables the identification of trapped states that exert influence below the lowest energy level of the conduction band in each specific case.

The process of calculating both electronic band structure and DOS first involves obtaining a converged density through a standard self-consistent field (SCF) calculation. Subsequently, this density is used to perform a non-self-consistent calculation to obtain the electronic band structure and DOS [64,79] for a selected k-path and an enriched uniform mesh respectively. It is crucial to note that the present study adheres to a theoretical framework, the study proposes that since electron traps in artificial materials are formed by impurities or structural defects they are related to the DOS. Specifically, high DOS at a specific energy level indicates the presence of traps responsible for these electron transitions. Moreover, it is indicated that high DOS could also be related to high electron traps concentration that leads to a higher TL intensity.

2.7. TL signal reconstruction based on OTOR

Thermoluminescence signal reconstruction, particularly within the framework of the One Trap One Recombination center model, involves a phenomenological process reliant on the electron band structure [31, 71]. Attention is directed toward identifying the lowest point of the dense conduction band limits, which serves as a reference for setting the minimum energy level. Below this threshold, each emerging energy state (due to doping) is deemed as an electron trap, TL analysis relates electron trap's energy level to be relative to the conduction band [80]. Estimating this minimum energy level value entails a statistical approach, which involves considering the repeatability of energy values representing the conduction band's dense zone. This statistical assessment ensures the robustness and reliability of the chosen energy threshold, facilitating accurate characterization of electron traps within the material.

Once the minimum energy level corresponding to the dense conduction band limit is established, the process advances to identifying electron traps based on the DOS diagram. The energy trap value is assessed by fitting each DOS curve and obtaining the mean value (in this case $\overline{E}$) through a Gaussian distribution. According to the OTOR model, electron traps, are located below that minimum energy level, and serve as sites capable of capturing electrons following radiation exposure. These trapped electrons remain localized until stimulated by a thermal or optical stimulus, leading to their subsequent release and emission of luminescence. Furthermore, the OTOR model provides a theoretical framework for interpreting the TL signal and trapping parameters. The peak characteristics and kinetics of this emitted TL signal offer insights about each material. By analyzing those characteristics, including peak temperatures (T_m), activation energies (E_a), and emission spectra (I_m), the underlying implications can be considered accordingly for various applications, ranging from material science, medical dosimetry to archaeological dating [71,73,78].

3. Results and discussion

3.1. Undoped beryllium oxide

In this configuration, an undoped beryllium oxide (*BeO*) with wurtzite structure was assumed, characterized by the following lattice parameters: a = 2.69 Å, b = 2.69 Å, c = 4.38 Å, with angles α and β equal to 90° and angle γ equal to 120°. These parameters were based on computational analysis and are consistent with those reported in the Materials Project database [67]. Specifically, the crystallographic data corresponds to the material identified by the Materials Project as mp-2542 (https://doi.org/10.17188/1200608), providing a reliable reference for the structural properties of BeO in its wurtzite phase. The calculated electronic band structure and density of states for *BeO* are depicted in Fig. 4.

In the undoped configuration, a direct bandgap is observed at the Γ point. The valence band is primarily constituted by $O\ p$ states, whereas the conduction band exhibits comparable proportions of *Be* and *O s* states, with a relatively higher amount of *Be* (red) compared to *O* (green). The energy bandgap of *BeO* was estimated to be 7.55 *eV*, demonstrating good agreement with the reported value of 7.46 eV (mp-2542). Thus, *BeO* is a wide bandgap insulator. Furthermore, the Fermi energy level was estimated to be at 4.93 *eV* above VBM. The location of E_{Fermi} is determined by charge neutrality, this ensuring that the total charge, including contributions from probable charged defects and any other type of carriers within the bands, balances out to zero. This principle is absent in insulators like *BeO* and maintains the material's electrical neutrality [79].

In this configuration, the reconstruction of the TL signal is not feasible due to the assumption of an undoped structure. The TL theory applies when forbidden energy levels attributable to a potential defect, impurity, or vacancy, which captures electrons after material's exposure to radiation. Since no defect, impurity, or vacancy has been considered in this case, the necessary conditions for TL signal reconstruction, such
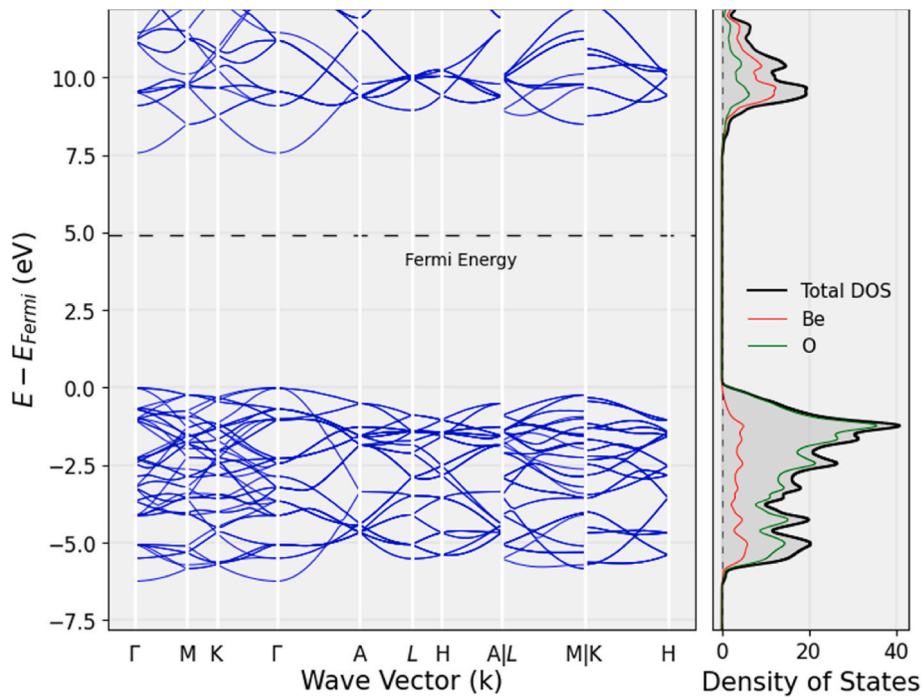
Fig. 4. (left) Electronic band structure and (right) Density of States of wurtzite BeO. The blue bands represent the energy valence and conduction bands (negative and positive energies respectively). The zero level in the energy scale is set at the Valence Band Maximum (VBM). On the right, the density of states is presented, as well as the atom projected DOS for Be and O atoms in different colors.

as the presence of trapping centers (electron traps), are not met. The TL signal reconstruction, in which the present study primarily focuses, is addressed for the other configurations.

3.2. Si-doped, and Si, Mg co-doped configuration

Two distinct approaches have been considered in this section, each

one investigating the intricate behavior of foreign atoms within the *BeO* crystal lattice. The first case entails the singular insertion of a *Si* atom that is effectively displacing a *Be* atom from its lattice position.

The calculated electronic band structure and density of states for *BeO* are depicted in Fig. 5.

In Fig. 5, it is evident that new states emerge following the insertion of a *Si* atom into the lattice. These states, while being absent in Fig. 4,
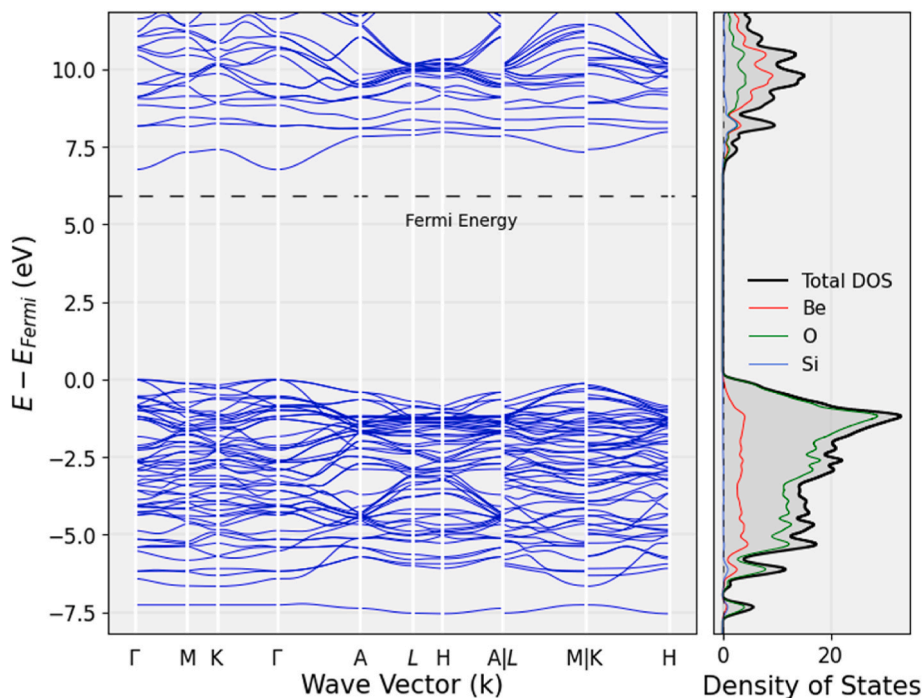
Fig. 5. (left) Electronic band structure and (right) total and atom projected DOS of Si doped BeO. The newly emerged states resulting from the addition of the Si dopant are shown in blue on the right graph.

manifest in the energy range around $\sim 7.5\ eV$. Positioned at the lower limit of the conduction band subsequent to displacing a *Be* atom, this area exhibits comparable proportions of *Be*, *O*, and *Si s* states, each present in similar amounts. The Fermi energy level is estimated to be 5.93 *eV*, slightly higher than the reported values ranging from 5.11 to 5.67 *eV*, potentially influenced by other defects [79,81]. Moreover, the energy band gap undergoes broadening, increasing by approximately 6% to 7.93 *eV* from the initial value of 7.46 *eV*.

The second case examines the coexistence of two substitutional atoms, namely *Si* and *Mg*, within the crystal lattice, further approaching the properties of BeO_T. Here, both *Si* and *Mg* atoms simultaneously replace two *Be* atoms. The calculated electronic band structure and density of states for *BeO* are depicted in Fig. 6.

In Fig. 6, the influence of *Mg* appears to be relatively negligible. Within the studied energy range, no discernible emergence of new states is observed, suggesting that *Mg* has minimal to no impact. Following the insertion of *Si* and *Mg* atoms into the lattice the same states as previously manifest around $\sim 7.5\ eV$, remain unaltered. The Fermi energy level is estimated to be 5.91 *eV*, in comparison with the previous value of 5.93 *eV*. The energy band gap also remains relatively unchanged at 7.94 *eV*. From this configuration, it can be safely stated that *Mg* appears to have minimal impact, particularly near the conduction band.

3.2.1. TL reconstruction of Si and Mg co-doped configuration

For the reconstruction of the TL signal based on the OTOR model, several initial parameters must be conditioned. These parameters include the energy associated with each electron trap, the initial concentrations of these traps denoted as $N\ (cm^{-3})$ with instantaneous occupancies represented by $n(t)$, and other parameters such as the frequency factor $s\ (s^{-1})$, and the kinetic order b. While the energy of each electron trap and the initial concentrations can be derived from DFT calculations and the DOS, the frequency factor and kinetic order need to be assumed from physical considerations. More precisely, as previously mentioned, the frequency factor (s) is linked to the Debye frequency, which characterizes the highest-frequency normal mode of atomic vibration in a solid, representing the upper limit of vibrational frequencies within the lattice [38]. For a glow-peak produced with

activation energy between 0.1 and 1.6 *eV*, the frequency factor corresponds to a value between 10^9 and $10^{13}\ s^{-1}$ [74–77]. Particularly, s corresponds to the frequency of thermal activation events involving each trap state. It can be conditioned based on existing reported experimental values or estimated for each thermal event. Opting for existing reported experimental values is usually advantageous since material properties and TL parameters have already been well-reported through literature [31]. While it's also possible to estimate values for each thermal event, typically corresponding to the temperature at which the TL signal emerges, firstly, is necessary to ensure an accurate representation of the crystal structure. Secondly, when estimating the frequency factor through phonon dispersion, it's essential to accurately correlate it with the normal modes for all branches and selected directions in the crystal.

Regarding the kinetic order b, it's noteworthy that beryllium oxide (BeO) demonstrates first-order kinetics behavior, akin to other artificial thermoluminescent dosimeters (TLDs) [5,7–14,17–20]. Therefore, a value between 1 and 1.1 has been also assumed for all cases in the present study. This value is in excellent agreement to the related literature, as it is well-reported that BeO predominantly exhibits first-order kinetics [7–14,17–20,42–44,46]. However, there are studies reporting that the second, high-temperature, TL peak may exhibit intermediate-order kinetics [11,12]. Nevertheless, for consistency and to align with the prominent assumptions in TL research, first-order kinetics were assumed in all cases unless a significant discrepancy between experimental and theoretical results was observed. In that case, a slight increase in the retrapping probability was assumed to account for a higher kinetic order value.

The experimental BeO TL curves presented in this section, which are used as a reference, were measured by our group and have been published in previous works; see Aşlar et al. (2019); Konstantinidis et al. (2020) and Polymeris et al. (2021) [11,42,43]. BeO doped with Si and Mg was used under controlled laboratory conditions. These data serve as a benchmark for comparing theoretical predictions based on DFT and OTOR simulations.

As evident in Fig. 7, the above plot showcases a narrowed area, present in the DOS graph, corresponding to the region below the
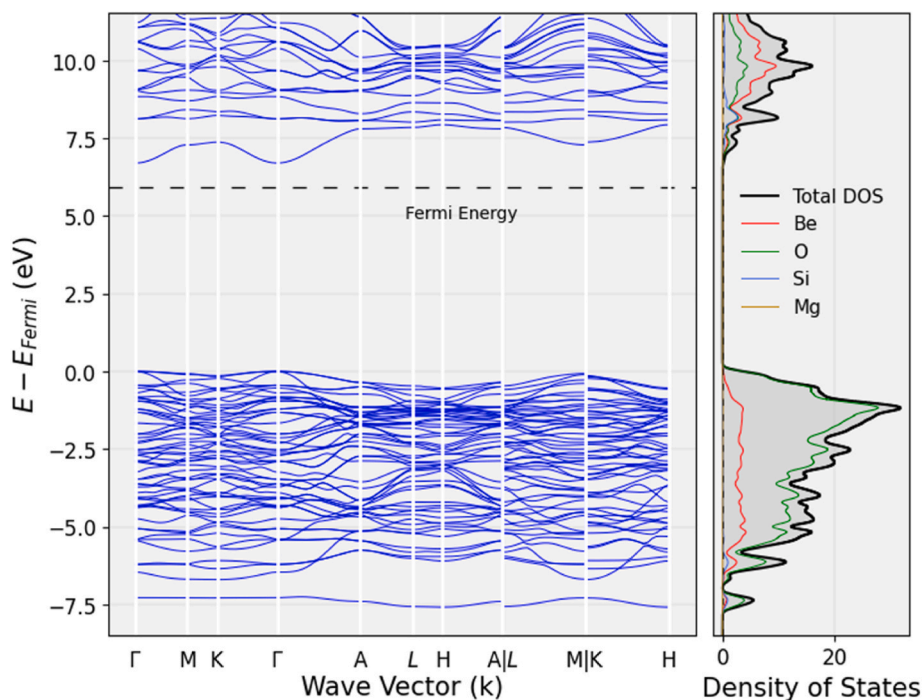
Fig. 6. (left) Electronic band structure and (right) total and atom projected DOS of Si, Mg doped BeO. The newly emerged states from the addition of the Si dopant are shown in blue, and those from the Mg dopant are shown in dark yellow, on the right graph.
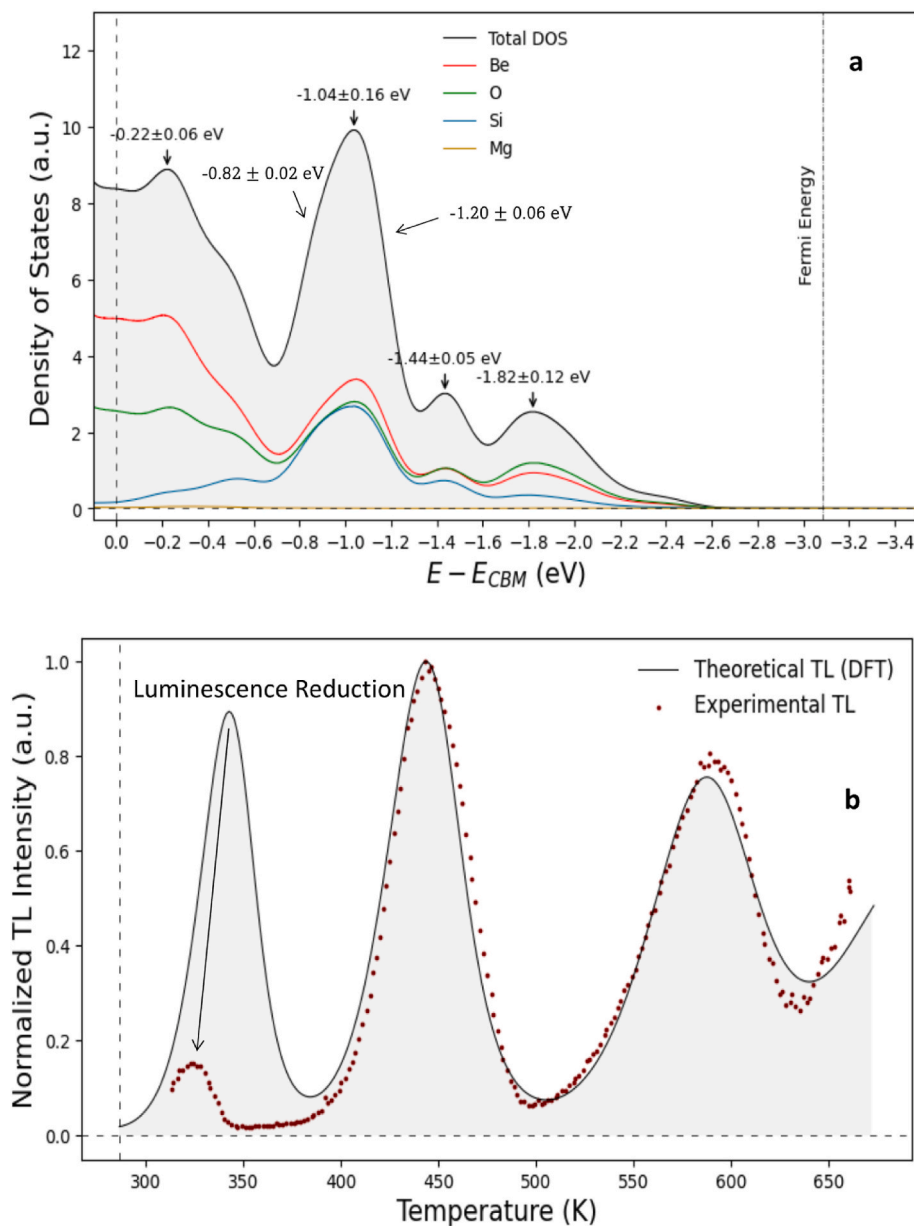
Fig. 7. (a) DOS of Si, Mg doped BeO that emerge below the conduction band and (b) the theoretical TL signal deriving through DFT calculations, along with the experimental TL signal deriving after 1 min of radiation exposure. The samples and literature data used in this experiment were BeO doped with Si and Mg, as published in Aşlar et al. (2019), Konstantinidis et al. (2020) and Polymeris et al. (2021) [11,42,43].

conduction band, as illustrated in the vertical plot of Fig. 6. In this plot, the lower limit of the conduction band serves as the reference point. Each state emerging below this threshold is denoted by negative values in order to signify their distance relative to the conduction band. This identification process is facilitated through the utilization of tools such as *scipy.signal.find_peaks*. Additionally, in cases where multiple DOS curves overlap, particularly evident in the energy region around $-1\ eV$, these overlapping values can be accurately extracted using Gaussian fitting techniques.

Regarding the TL signal reconstruction in Fig. 7b, the process begins by identifying the maximum DOS value on the y-axis, which correlates with the concentration of electrons at a specific energy level. Simultaneously, the energy, in which that maximum responds, is determined and represents the activation energy of the trap. These two values serve as initial conditions for the OTOR model. However, since the DOS graph provides arbitrary units on the y-axis, normalization of TL intensity is necessary to establish a direct correlation between photon emission and

electron trap concentration. Normalization is achieved by dividing each data point by the maximum intensity value of the entire TL glow curve, resulting in a final TL plot where intensity values range between 0 and 1. The same process was also applied to the experimental data, as depicted in Fig. 7b. This approach ensures that TL intensity accurately corresponds to the photon emission originating from these traps. By normalizing the TL intensity values, the experimental measurements become more easily correlated with the reconstructed TL signal.

In both theoretical and experimental TL signals, the temperature ranges from 300 to 650 K, which corresponds to the operational temperature range of the Harsaw Thermoluminescent Dosimeter (TLD) reader. In this range three prominent TL peaks emerge: the 1st peak occurs around $\sim 340\ K$, the 2nd peak at approximately 450 K, and the 3rd peak near $\sim 590\ K$. These peaks signify specific energy levels at which trapped electrons are thermally released, leading to luminescence emission.

Theoretical predictions based on the DOS suggest the presence of

electron traps near 7 eV from the VBM, corresponding to the energy levels responsible for the TL peaks observed experimentally. The close alignment of peak temperatures between theoretical (347 K, 448 K, 585 K) and experimental (334 K, 449 K, 587 K) data further validates the accuracy of our model. The visual representation in Fig. 6b highlights a noteworthy observation, the alignment of TL peaks between theoretical and experimental data is remarkably close. However, a notable discrepancy arises in the experimental TL data, particularly in the intensity of the 1st peak. In comparison to the theoretical predictions, the intensity of the 1st peak exhibits a luminescence intensity reduction.

The observed reduction in the intensity of the first TL peak in the experimental data is attributed to the nature of the corresponding trap. Since the delocalization temperature is around 350 K, the trap is shallow and has a short lifetime. Essentially, the thermal vibrational modes at room temperature facilitates the pre-release of a large fraction of trapped electrons, even at ambient temperature, resulting in a decrease in the overall TL intensity associated with this specific peak. This reduction underscores the importance of considering environmental factors and pre-existing conditions when interpreting TL data, especially in materials with intricate trapping and recombination mechanisms.

Finally, the validation of both theoretical and experimental TL signals was achieved through the analysis methods of CGCD and PSM. While CGCD is applicable across all cases, as it effectively deconvolves each TL peak, enabling comprehensive analysis, PSM is specifically employed for TL peaks that do not overlap. In this approach, each peak is analyzed separately to ensure accurate validation. These validation results are depicted in Table 1.

The comparison between experimental and theoretical results reveals a close alignment, with values falling within a small deviation of approximately ∼ 1 - 2%. Both the CGCD and PSM effectively validate the initial conditions, further reinforcing the theoretical framework of the present study. Furthermore, the temperature values corresponding to the maximum intensity of the TL peaks, were found to closely align with the actual experimental values. The accuracy and reliability of these TL signals further justify the predictive capabilities of the present protocol.

3.3. Cr-doped, and Cr, Mg co-doped configuration

As outlined in Section 3.2, two distinct approaches have also been explored here, each one investigating the interactions of foreign atoms within the *BeO* crystal lattice. The first case entails the singular insertion of a *Cr* atom that is displacing a *Be* atom from its lattice position.

The calculated electronic band structure and density of states for *BeO* are depicted in Fig. 8.

In Fig. 8, once again new states emerge following the insertion of a *Cr* atom into the lattice. These states are absent in Fig. 4 and manifest in the energy range around ∼ 7.5 *eV*. This area exhibits comparable proportions of *Be*, *O*, while closer to the lower limit of the conduction band, higher proportions of *Cr s* states seem to emerge. The estimated Fermi energy level is 5.43 *eV*, falling within the reported range of values from 5.11 to 5.67 *eV* [79]. However, in this case the energy band gap experiences a slight narrowing, decreasing by approximately 7% to 6.93 *eV*

Table 1
Activation energy of the trap (eV) and Temperature (K) in BeO:Si,Mg and Themalox 995.

BeO: Si, Mg	Activation Energy (eV), Temperature (K)		
	Experimental (Thermalox 995)		Theoretical (DOS - OTOR)
	CGCD	PSM	
Peak #1	0.85 ± 0.01 eV, 334 K	0.84 ± 0.02 eV, 334 K	0.82 ± 0.02 eV, 347 K
Peak #2	1.04 ± 0.02 eV, 449 K	1.05 ± 0.01 eV, 449 K	1.04 ± 0.07 eV, 448 K
Peak #3	1.23 ± 0.02 eV, 587 K	1.23 ± 0.04 eV, 586 K	1.20 ± 0.06 eV, 585 K

from its initial value of 7.46 *eV*.

The second case examines the coexistence of two substitutional atoms, *Cr* and *Mg*, simultaneously replacing two *Be* atoms within the crystal lattice. This configuration emulates the properties of BeO_R, as reported by Aşlar et al. (2021) and Konstantinidis et al. (2022) [44,47]. The calculated electronic band structure and density of states for *BeO* are depicted in Fig. 9.

In Fig. 9, similar to the *Si*, *Mg* configuration, the presence of *Mg* appears to have no negligible impact on the energy states, reinforcing that particular conclusion. After introducing *Cr* and *Mg* atoms into the lattice, similar states as before are observed around ∼ 7 *eV*. Nevertheless, the Fermi energy level is estimated to be 5.33 *eV*, showing a slight decrease compared to the previous value of 5.43 *eV*. However, there is a slight increase in the energy band gap, reaching 7.04 *eV*, which reduces the previous deviation to approximately ∼ 5.8 %.

Based on the findings from both configurations outlined in Sections 3.2 and 3.3, it is clear that *Mg* exerts minimal influence. To dispel any uncertainties, the configuration involving a single Mg dopant was also examined. It was determined that the presence of *Mg* within the *BeO* crystal lattice has little to no effect, especially near the lower limit of the conduction band, which is the primary focus of this study.

High levels of Mg doping may influence the TL behavior through indirect mechanisms, even if the direct impact on the density of states (DOS) appears minimal. One potential mechanism is lattice strain, as the incorporation of Mg atoms compared to the host material can distort the crystal lattice. This strain can alter the local electronic environment, affecting charge carrier mobility and trapping centers, which are crucial for TL processes. Additionally, higher Mg concentrations may lead to defect formation, such as vacancies or interstitials, which could introduce new energy states or modify existing traps. These lattice distortions and defects, while not prominently reflected in the DOS, may still play a significant role in modulating TL behavior by influencing the energy levels available for charge carrier recombination and trapping.

3.3.1. TL reconstruction of Cr and Mg co-doped configuration

Following the same theoretical procedure as detailed in Section 3.2.1, the TL signal was reconstructed using the OTOR model. In this process, the initial parameters were adjusted based on insights obtained from the DOS diagram. This adjustment ensured that the parameters were appropriately set to accurately reflect the electronic structure and energy distribution. Specifically, the energy associated with each electron trap (E_α), the initial concentrations of these traps denoted as $N\ (cm^{-3})$ with instantaneous occupancies represented by $n(t)$, and the frequency factor $s\ (s^{-1})$, and kinetic order b.

The experimental TL glow curves for Cr and Mg co-doped BeO, presented here, were also measured by our group and were previously reported by Aşlar et al. (2019, 2021, 2022) and Konstantinidis et al. (2022) [11,12,44,47]. These literature data, as already mentioned, allow for direct comparison with our theoretical reconstructions to validate the model's predictive capabilities.

In Fig. 10b, the TL signal reconstruction process initiates by identifying the peak DOS value on the y-axis, corresponding to the electron concentration at a specific energy level. Initially, the energy values were identified, followed by the normalization of the TL intensity over the maximum corresponding value. This normalization process resulted in a final TL plot where the intensity values were scaled to range between 0 and 1.

The temperature ranges from 0 to 650 K, aligning with the operational temperature range of the TLD reader. In this range three prominent TL peaks emerge: the 1st peak occurs around 440 *K*, the 2nd peak at ∼ 475 *K*, and the 3rd peak near ∼ 590 *K*. In contrast to Fig. 6b, Fig. 9b displays a noticeable deviation between the theoretical and experimental TL signals, making this particular case more challenging to accurately evaluate.

The theoretical TL signals correspond well to the experimental peaks
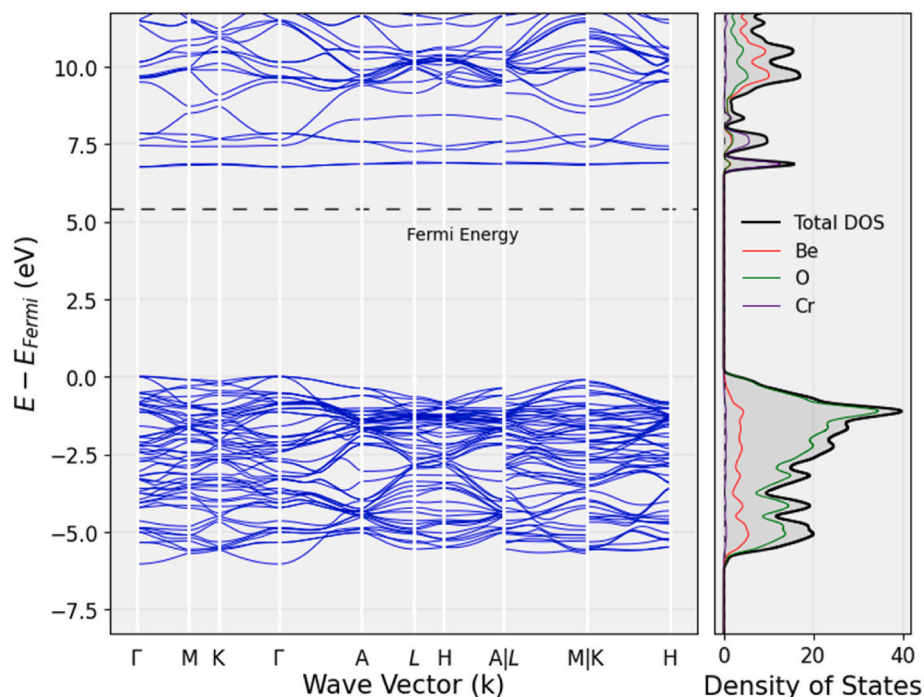
Fig. 8. (left) Electronic band structure and (right) total and atom projected DOS of Cr doped BeO. The newly emerged states resulting from the addition of the Cr dopant are shown in purple on the right graph.
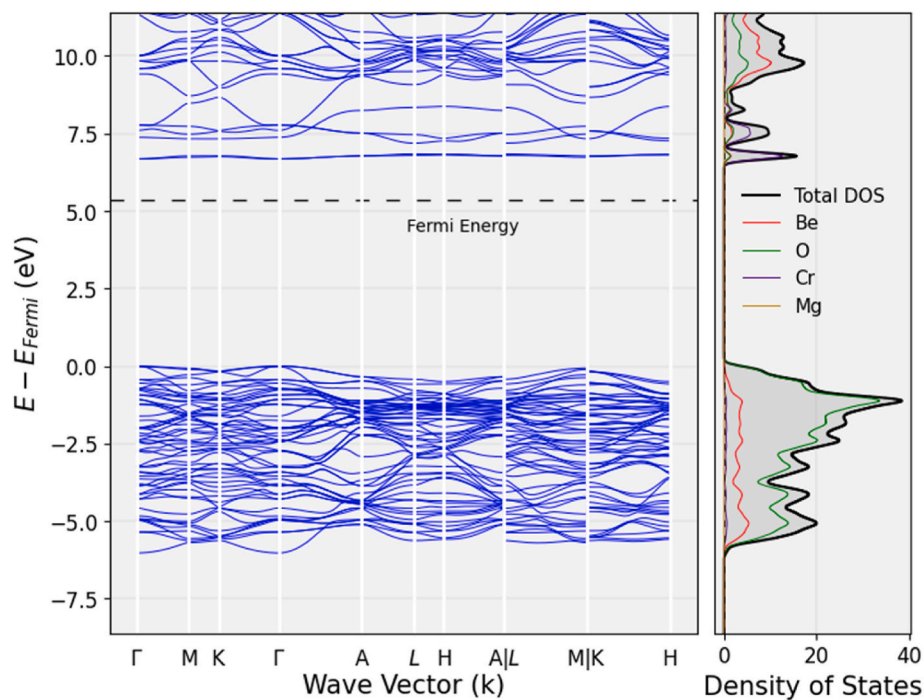
Fig. 9. (left) Electronic band structure and (right) total and atom projected DOS of Cr, Mg doped BeO. The newly emerged states from the addition of the Cr dopant are shown in purple, and those from the Mg dopant are shown in dark yellow, on the right graph.

at 440 K and 590 K, though the broader experimental peaks suggest the need to consider other attributes. The introduction of *Cr* states near 7 eV from the valence band significantly affects electron trapping, as evidenced by the 1st TL peak. Specifically, the experimental 1st peak appears slightly broader compared to the theoretical peak. Several factors could account for this observation, with the most likely explanation being the kinetics behavior. While the theoretical model assumes first-

order kinetics in all cases, experimental observations suggest that the 1st peak most probably exhibits an intermediate order of kinetics [44, 47]. Additionally, discrepancies in the actual structure compared to the simulation, or the presence of other dopants such as *Sn* or *Er* in the material, could contribute to the differences observed in the final TL signal [44].

The theoretical and experimental TL signals were validated using
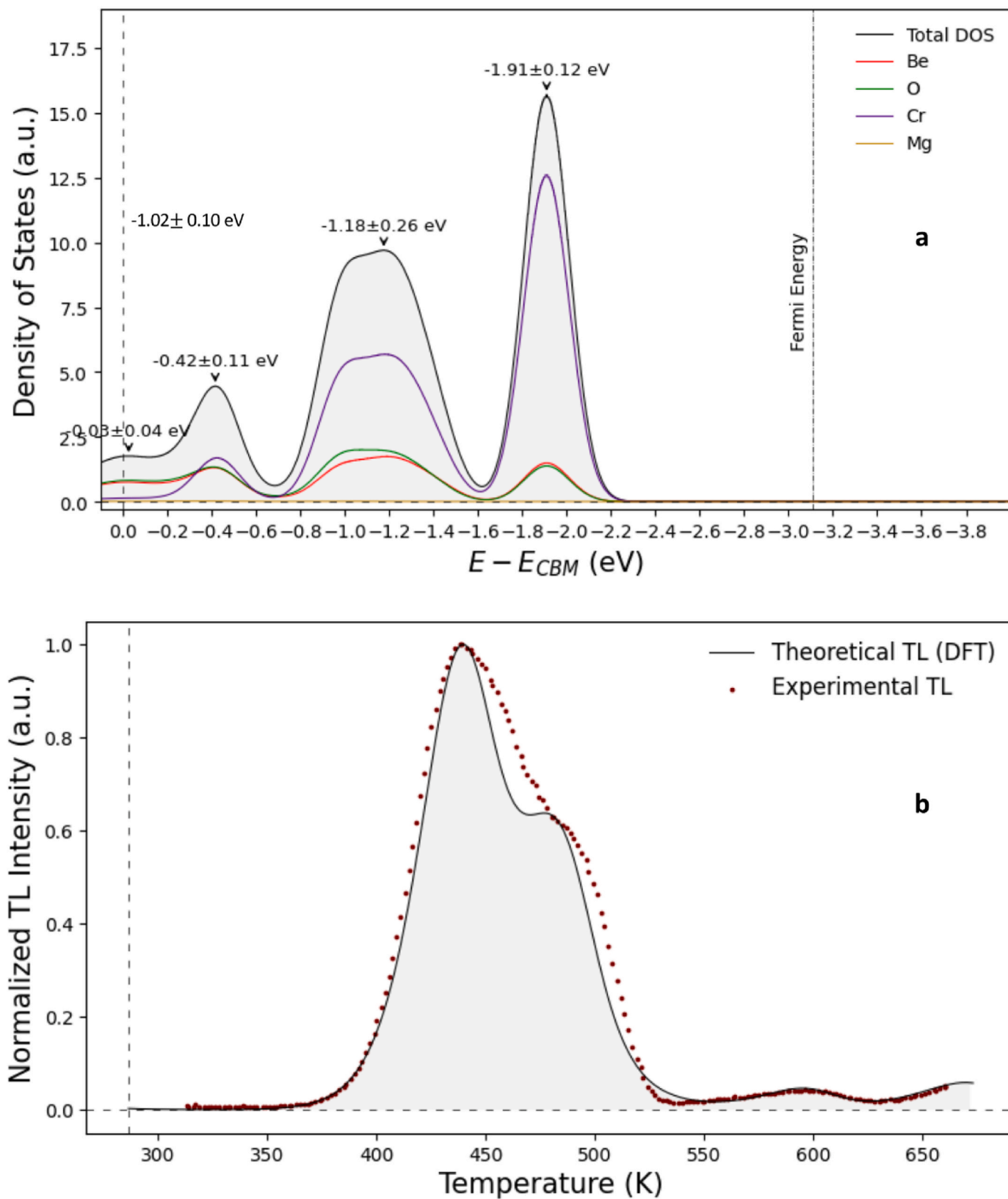
Fig. 10. (a) DOS of Cr, Mg doped BeO that emerge below the conduction band and (b) the theoretical TL signal deriving through DFT calculations, along with the experimental TL signal deriving after 1 min of radiation exposure. The samples and literature data used in this experiment were BeO doped with Cr and Mg, as published in Aşlar et al. (2019, 2021, 2022) and Konstantinidis et al. (2022) [11,12,44,47].

Table 2

Activation energy of the trap (eV) and Temperature (K) in BeO:Cr,Mg and Radkor.

BeO: Cr, Mg	Activation Energy (eV), Temperature (K)		
	Experimental (Radkor)		Theoretical (DOS - OTOR)
	CGCD	PSM	
Peak #1	1.02 ± 0.12 eV, 442 K	–	1.02 ± 0.10 eV, 436 K
Peak #2	1.18 ± 0.08 eV, 472 K	–	1.18 ± 0.26 eV, 469 K
Peak #3	1.93 ± 0.09 eV, 587 K	1.90 ± 0.09 eV, 586 K	1.91 ± 0.12 eV, 588 K

both CGCD and PSM techniques, wher possible. As previously mentioned, CGCD, which deconvolves each TL peak, allows for comprehensive analysis and is applicable to all cases. Conversely, PSM is utilized for TL peaks without overlap. The results of these validation methods are presented in Table 2.

In this specific instance, although the theoretical values align, falling within a small deviation of approximately ~ 1 - 2% with the experimental values, the influence of other parameters complicates the TL reconstruction process. Due to the overlap of Peak #1 and Peak #2, PSM could not estimate the activation energy corresponding to these states. Nevertheless, the CGCD effectively validates the initial conditions. Concerning the temperature point associated with each peak, the experimental signal shows higher readings compared to the theoretical signal derived from OTOR. This suggests that due to the broadened signal, a slightly higher temperature is required before electron recombination initiates. Especially for this case, it is essential to explore additional adjustments or alternative configurations to further refine the existing protocol without overlooking the computational cost of the process.

4. Conclusions

The aim of the present study is to examine the electronic band structure and density of states of Beryllium Oxide (*BeO*) and the effect of substitutional *Si*, *Mg* and *Cr* doping on *BeO*, by employing DFT, in conjunction with the OTOR model as an alternative approach to TL analysis. Various configurations were examined with the aim of simulating the TLD structures of Thermalox 995 and Radkor. Initially, the supercell size was defined, and its structure optimized, followed by an investigation into the undoped *BeO* structure. The results showed good agreement with values reported in the literature. Two distinct cases were analyzed: the *Si*-doped and *Si-Mg* co-doped configuration, and the *Cr*-doped and *Cr-Mg* co-doped configuration. Despite multiple adjustments, DFT calculations demonstrated that the specific location of the dopant had minimal impact on the overall results. In both cases, the insertion of *Si* or *Cr* appeared to have the most significant effect on the DOS and band structure, while *Mg* showed negligible impact. To confirm this observation, a *BeO* configuration doped with *Mg* only was explored, further supporting the conclusion that *Mg* had minimal impact, especially near the lower limit of the conduction band.

The obtained results served as initial conditions for the OTOR model's differential equations 5–13 to theoretically and qualitatively reconstruct the TL signals. These signals were compared with actual experimental measurements, and electron trapping parameters on both reconstructed and experimental results were validated through CGCD and PSM. TL signals were displayed for both cases within the temperature range of $0 - 650\,K$, the operational temperature range of TLD reader. In the first case, three prominent TL peaks were observed, with temperatures around $340\,K$, $450\,K$, and $590\,K$. While the theoretical and experimental TL peaks aligned well, a reduction in intensity was observed for the experimental 1st peak, attributed to ambient room temperature's influence in releasing trapped electrons. In the second

case, again three prominent TL peaks were observed, with temperatures around $440\,K$, $475\,K$, and $590\,K$. Unlike the first case, a noticeable deviation between theoretical and experimental TL signals was observed, with the experimental 1st peak appearing slightly broader than the theoretical peak. Several factors, including the material's intermediate kinetics behavior and the presence of other dopants contributing to the final TL signal, may be responsible for this deviation. Thermalox 995, due to its high purity and fewer secondary dopants, was less demanding on its simulation conditions compared to the more complex structure of Radkor.

Overall, the employed theoretical framework successfully demonstrated the feasibility of simulating TL behavior. However, further investigation and additional research is needed in order to ensure further understanding and practical applications. In particular, it is essential to verify the consistency of results for larger crystal structures exceeding dimensions of $3 \times 3 \times 1$ and higher k points, while exploring the potential contributions of other calculations, such as phonon density of states or the temperature dependance of density of states, to the reconstruction process. Phonons, representing thermal lattice vibrations at ambient temperatures, play a crucial role in influencing charge carrier dynamics, particularly in materials where lattice vibrations affect trapping and recombination processes. Incorporating phonon DOS enables the capture of interactions between lattice vibrations and electronic states. This approach not only enhances the understanding of the frequency factor, a parameter with significant impact on TL research, but also aids in its validation. Additionally, temperature-dependent calculations could account for shifts in energy levels and trap states as the material is heated, refining the modeling of TL glow curves under varying thermal conditions. This approach could bridge the gap between theoretical simulations and experimental observations, leading to more precise predictions of TL phenomena.

Finally, investigations into larger structures, coupled with the simultaneous addition of other dopants, may offer valuable insights into their experimental TL properties while also extend the understanding of experimental TL research.

CRediT authorship contribution statement

E. Tsoutsoumanos: Writing – review & editing, Writing – original draft, Visualization, Methodology, Investigation, Formal analysis, Conceptualization. **D. Tzeli:** Writing – review & editing, Validation, Methodology, Investigation, Conceptualization. **A. Avramopoulos:** Writing – review & editing, Validation, Methodology, Investigation, Conceptualization. **N. Laskaris:** Writing – review & editing, Validation, Methodology, Investigation, Conceptualization. **P.G. Konstantinidis:** Writing – review & editing, Methodology, Investigation, Formal analysis. **E. Travlou:** Methodology, Investigation, Formal analysis. **N. Korakis:** Visualization, Methodology, Investigation, Formal analysis. **N.N. Lathiotakis:** Writing – review & editing, Validation, Methodology, Investigation, Conceptualization. **G. Kitis:** Writing – review & editing, Validation, Methodology, Investigation, Conceptualization. **G.S. Polymeris:** Writing – review & editing, Validation, Supervision, Methodology, Investigation, Conceptualization. **T. Karakasidis:** Writing – review & editing, Validation, Supervision, Methodology, Investigation, Conceptualization.

Declaration of competing interest

The authors declare that they have no known competing financial interests or personal relationships that could have appeared to influence the work reported in this paper.

Data availability

Data will be made available on request.

References

[1] A.J.J. Bos, Theory of thermoluminescence, Radiat. Meas. 41 (2006) S45–S56, https://doi.org/10.1016/j.radmeas.2007.01.003.

[2] F. Daniels, C.A. Boyd, D.F. Saunders, "Thermoluminescence as a research tool, Science" 117 (3040) (1953) 343–349, https://doi.org/10.1126/science.117.3040.343.

[3] A.J.J. Bos, High sensitivity thermoluminescence dosimetry, Nucl. Instrum. Methods Phys. Res. Sect. B Beam Interact. Mater. Atoms 184 (1–2) (2001) 3–28, https://doi.org/10.1016/s0168-583x(01)00717-0.

[4] C.E. Mandeville, H.O. Albrecht, Luminescence of beryllium oxide, Phys. Rev. 94 (1954) 494, https://doi.org/10.1103/PhysRev.94.494.

[5] E. Tsoutsoumanos, M. Saleh, P.G. Konstantinidis, V. Altunal, P.D. Sahare, Z. Yegingil, T. Karakasidis, G. Kitis, G.S. Polymeris, Nanostructured TLDs: studying the impact of crystalline size on the Thermoluminescence glow-curve shape and electron trapping parameters, Radiat. Phys. Chem. 212 (2023) 111067, https://doi.org/10.1016/j.radphyschem.2023.111067.

[6] S.W.S. McKeever, M. Moscovitch, P.D. Townsend, Thermoluminescence dosimetry materials: properties and uses, Ashford, Nuclear Technology Publishing, 1995, p. 210. ISBN:1870965191.

[7] D.R. Vij, N. Singh, Thermoluminescence dosimetric properties of beryllium oxide, J. Mater. Sci. 32 (1997) 2791–2796, https://doi.org/10.1023/A:1018608113663.

[8] E. Bulur, H. Göksu, OSL from BeO ceramics: new observations from an old material, Radiat. Meas. 29 (6) (1998) 639–650, https://doi.org/10.1016/S1350-4487(98)00084-5.

[9] E.G. Yukihara, Observation of strong thermally transferred optically stimulated luminescence (TT-OSL) in BeO, Radiat. Meas. 121 (2019) 103–108, https://doi.org/10.1016/j.radmeas.2018.12.014.

[10] E.G. Yukihara, Characterization of the thermally transferred optically stimulated luminescence (TT-OSL) of BeO, Radiat. Meas. 126 (2019) 106132, https://doi.org/10.1016/j.radmeas.2019.106132.

[11] E. Aşlar, N. Meriç, E. Şahiner, O. Erdem, G. Kitis, G.S. Polymeris, A correlation study on the TL, OSL and ESR signals in commercial BeO dosimeters yielding intense transfer effects, J. Lumin. 24 (2019) 116533, https://doi.org/10.1016/j.jlumin.2019.116533.

[12] E. Aşlar, E. Şahiner, G.S. Polymeris, N. Meriç, Thermally and optically stimulated luminescence properties of BeO dosimeter with different main dosimetric peak, Appl. Radiat. Isot. 170 (2021) 109635, https://doi.org/10.1016/j.apradiso.2021.109635.

[13] E. Bulur, Photo-transferred luminescence from BeO ceramics, Radiat. Meas. 42 (2007) 334–340, https://doi.org/10.1016/j.radmeas.2007.02.065.

[14] E. Bulur, B.E. Saraç, Time-resolved OSL studies on BeO ceramics, Radiat. Meas. 59 (2013) 129–138, https://doi.org/10.1016/j.radmeas.2013.04.009.

[15] S.V. Nikiforov, I.G. Avdyushin, D.V. Ananchenko, A.N. Kiryakov, A.F. Nikiforov, Thermoluminescence of new Al2O3-BeO ceramics after exposure to high radiation doses, Appl. Radiat. Isot. 141 (2018) 15–20, https://doi.org/10.1016/j.apradiso.2018.08.003.

[16] S.V. Nikiforov, A.D. Borbolin, A. Yu Marfin, D.V. Ananchenko, S.V. Zvonarev, New luminescent ceramics based on anion-deficient Al2O3–BeO for high-dose dosimetry, Radiat. Meas. 134 (2020) 106303, https://doi.org/10.1016/j.radmeas.2020.106303.

[17] E. Aşlar, E. Şahiner, G.S. Polymeris, N. Meriç, Feasibility of determining Entrance Surface Dose (ESD) and mean glandular dose (MGD) using OSL signal from BeO dosimeters in mammography, Radiat. Phys. Chem. 177 (2020) 109151, https://doi.org/10.1016/j.radphyschem.2020.109151.

[18] E. Yukihara, A review on the OSL of BeO in light of recent discoveries: the missing piece of the puzzle? Radiat. Meas. 134 (2020) 106291 https://doi.org/10.1016/j.radmeas.2020.106291.

[19] E. Aşlar, N. Meriç, E. Şahiner, G. Kitis, G.S. Polymeris, Calculation of thermal quenching parameters in BeO ceramics using solely TL measurements, Radiat. Meas. 103 (2017) 13–25, https://doi.org/10.1016/j.radmeas.2017.06.011.

[20] E. Aşlar, E. Şahiner, G.S. Polymeris, N. Meriç, Determination of trapping parameters in BeO ceramics in both quenched as well as reconstructed thermoluminescence glow using various analysis methods, Appl. Radiat. Isot. 129 (2017) 142–151, https://doi.org/10.1016/j.apradiso.2017.08.026.

[21] V.S. Kortov, I.I. Milman, S.V. Nikiforov, E.V. Moiseĭkin, Mechanism of formation of nonlinearity in the dose dependence of the thermoluminescence output for anion-defect α-Al 2 O 3 crystals, Phys. Solid State 48 (3) (2006) 447–452, https://doi.org/10.1134/S1063783406030073.

[22] D.G. Kellerman, M. Kalinkin, R. Abashev, N.I. Medvedeva, A. Surdo, A. P. Tyutyunnik, Unusual intrinsic thermoluminescence in LiMgPO4:Er, Phys. Chem. Chem. Phys. 22 (2020) 27632–27644, https://doi.org/10.1039/d0cp05185c.

[23] K.R. Sature, B.J. Patil, S.S. Dahiwale, V.N. Bhoraskar, S.D. Dhole, Development of computer code for deconvolution of thermoluminescence glow curve and DFT simulation, J. Lumin. 192 (2017) 486–495, https://doi.org/10.1016/j.jlumin.2017.06.016.

[24] N.T. Mandlik, S.R. Rondiya, N.Y. Dzade, M.S. Kulkarni, P.D. Sahare, B.C. Bhatt, S. D. Dhole, Thermoluminescence, photoluminescence and optically stimulated luminescence characteristics of CaSO4:Eu phosphor: experimental and density functional theory (DFT) investigations, J. Lumin. 221 (2020) 117051, https://doi.org/10.1016/j.jlumin.2020.117051.

[25] T.B. Bekker, A.P. Yelisseyev, V.P. Solntsev, A.V. Davydov, T.M. Inerbaev, S. V. Rashchenko, A.I. Kostyukov, The influence of co-doping on the luminescence and thermoluminescence properties of Cu-containing fluoride borate crystals, CrystEngComm 23 (2021) 6599–6609, https://doi.org/10.1039/D1CE00556A.

[26] P.K. Jangid, G. Arora, D. Mali, P.K. Joshi, K. Kumar, B.L. Ahuja, First principles calculations to probe electronic response of lithium tetraborate, J. Phys. Conf. 1504 (2020) 012017, https://doi.org/10.1088/1742-6596/1504/1/012017.

[27] M. El-Kinawy, F. Abdel-Wahab, N. Seriani, N. El-Faramawy, DFT study of the role of point and complex defects on luminescence, electronic, and thermodynamic properties of LiF: Mg, Mater. Res. Bull. 158 (2023) 112044, https://doi.org/10.1016/j.materresbull.2022.112044.

[28] P. Modak, B. Modak, Insight into enhanced thermoluminescence property of (Mg, Cu, Ag)-Doped LiF:A DFT study, J. Lumin. 231 (2021) 117779, https://doi.org/10.1016/j.jlumin.2020.117779.

[29] V. Pagonis, R. Chen, Monte Carlo simulations of TL and OSL in nanodosimetric materials and feldspars, Radiat. Meas. 81 (2015) 262–269, https://doi.org/10.1016/j.radmeas.2014.12.009.

[30] V. Pagonis, P. Truong, Thermoluminescence due to tunneling in nanodosimetric materials: a Monte Carlo study, Phys. B Condens. Matter 531 (2018) 171–179, https://doi.org/10.1016/j.physb.2017.12.042.

[31] G. Kitis, G.S. Polymeris, V. Pagonis, Stimulated luminescence emission: from phenomenological models to master analytical equations, Appl. Radiat. Isot. 153 (May) (2019) 108797, https://doi.org/10.1016/j.apradiso.2019.05.041.

[32] G. Kitis, A. Sadek, G. Polymeris, V. Pagonis, Simulation of the effect of resolution between thermoluminescence peaks on the initial rise method of analysis, Nucl. Instruments Methods Phys. Res. Sect. B Beam Interact. with Mater. Atoms 524 (March) (2022) 1–7, https://doi.org/10.1016/j.nimb.2022.05.004.

[33] E. Tsoutsoumanos, P.G. Konstantinidis, G.S. Polymeris, T. Karakasidis, G. Kitis, Electron trap filling and emptying through simulations: studying the shift of the maximum intensity position in Thermoluminescence and Linearly Modulated Optically Stimulated Luminescence curves, Radiat. Meas. 153 (2022) 106735, https://doi.org/10.1016/j.radmeas.2022.106735. November 2021.

[34] G. Kitis, V. Pagonis, On the need for deconvolution analysis of experimental and simulated thermoluminescence glow curves, Materials 16 (2) (2023) 1–16, https://doi.org/10.3390/ma16020871.

[35] B. Subedi, G. Kitis, V. Pagonis, Simulation of the influence of thermal quenching on thermoluminescence glow-peaks, Phys. Status Solidi Appl. Mater. Sci. 207 (5) (2010) 1216–1226, https://doi.org/10.1002/pssa.200925588.

[36] P. Mobit, Y.S. Horowitz, L. Oster, The use of Monte Carlo simulations for accurate dose determination with thermoluminescence dosemeters in radiation therapy beams, Radiat. Prot. Dosimetry 101 (1–4) (2002) 383–386, https://doi.org/10.1093/oxfordjournals.rpd.a006007.

[37] V. Pagonis, Luminescence Data Analysis and Modeling Using R, Springer, 2021, https://doi.org/10.1007/978-3-030-67311-6.

[38] R. Chen, V. Pagonis, The role of simulations in the study of thermoluminescence (TL), Radiat. Meas. 71 (2014) 8–14, https://doi.org/10.1016/j.radmeas.2013.12.011.

[39] N. Gemechu, T. Senbeta, B. Mesfin, V.N. Mal'Nev, Thermoluminescence from silicon quantum dots in the two traps–one recombination center model, Ukr. J. Phys. 62 (2) (2017) 140–145, https://doi.org/10.15407/ujpe62.02.0140.

[40] J.F. Benavente, J.M. Gómez-Ros, A.M. Romero, Numerical analysis of the irradiation and heating processes of thermoluminescent materials, Radiat. Phys. Chem. 170 (July 2019) (2020) 108671, https://doi.org/10.1016/j.radphyschem.2019.108671.

[41] A.S. Merezhnikov, S.V. Nikiforov, V. Pagonis, Simulation of TL kinetics in complex trap cluster systems: some new approaches, Radiat. Meas. 125 (December 2018) (2019) 78–84, https://doi.org/10.1016/j.radmeas.2019.04.021.

[42] P. Konstantinidis, E. Tsoutsoumanos, G.S. Polymeris, G. Kitis, Thermoluminescence response of various dosimeters as a function of irradiation temperature, Radiat. Phys. Chem. 177 (July) (2020) 109156, https://doi.org/10.1016/j.radphyschem.2020.109156.

[43] G.S. Polymeris, S. Çoskun, E. Tsoutsoumanos, P.G. Konstantinidis, E. Aşlar, E. Şahiner, N. Meriç, G. Kitis, Dose response features of quenched and reconstructed, TL and deconvolved OSL signals in BeO, Results Phys. 25 (2021) 104222, https://doi.org/10.1016/j.rinp.2021.104222.

[44] P.G. Konstantinidis, E. Tsoutsoumanos, G.S. Polymeris, G. Kitis, Recombination pathways in a BeO yielding two main dosimetric TL peaks, Radiat. Meas. 151 (November 2021) (2022) 106716, https://doi.org/10.1016/j.radmeas.2022.106716.

[45] S. Watanabe, T.K. Gundu Rao, P.S. Page, B.C. Bhatt, TL, OSL and ESR studies on beryllium oxide, J. Lumin. 130 (11) (2010) 2146–2152, https://doi.org/10.1016/j.jlumin.2010.06.009.

[46] G.S. Polymeris, Thermally assisted optically stimulated luminescence (TA-OSL) from commercial BeO dosimeters, Materials 16 (4) (2023) 1494, https://doi.org/10.3390/ma16041494.

[47] E. Aşlar, E. Şahiner, G.S. Polymeris, N. Meriç, Thermally and optically stimulated luminescence properties of BeO dosimeter with double TL peak in the main dosimetric region, Appl. Radiat. Isot. 170 (2021) 109635, https://doi.org/10.1016/j.apradiso.2021.109635.

[48] E. Kara, A. Hicsonmez, Physical and dosimetric characteristic properties of BeO OSL for clinical dosimetric measurements, Appl. Radiat. Isot. 186 (2022) 110199, https://doi.org/10.1016/j.apradiso.2022.110199.

[49] A.M.C. Santos, M. Mohammadi, V.S. Afshar, Evaluation of a real-time BeO ceramic fiber-coupled luminescence dosimetry system for dose verification of high dose rate brachytherapy, Med. Phys. 42 (2015) 6349–6356, https://doi.org/10.1118/1.4931968.

[50] N. Abdullah, B.J. Abdullah, H. Rshid, C.S. Tang, A. Manolescu, V. Gudmundsson, Enhanced electronic and optical responses of nitrogen- or boron-doped BeO monolayer: first principle computation, Superlattice. Microst. 162 (2022) 107102, https://doi.org/10.1016/j.spmi.2021.107102.

[51] M. Gorbunova, I. Shein, Y. Makurin, V. Ivanovskaya, V. Kijko, A. Ivanovskii, Electronic structure and magnetism in BeO nanotubes induced by boron, carbon and nitrogen doping, and beryllium and oxygen vacancies inside tube walls, Phys. E Low-dimens. Syst. Nanostruct. 41 (1) (2008) 164–168, https://doi.org/10.1016/j.physe.2008.07.002.

[52] N.R. Abdullah, B.J. Abdullah, V. Gudmundsson, High thermoelectric and optical conductivity driven by the interaction of Boron and Nitrogen dopant atoms with a 2D monolayer Beryllium Oxide, Mater. Sci. Semicond. Process. 141 (2022) 106409, https://doi.org/10.1016/j.mssp.2021.106409.

[53] Y. Liu, X. Liu, M. Chen, Copper-doped beryllium and beryllium oxide interface: a first-principles study, J. Nucl. Mater. 545 (2021) 152733, https://doi.org/10.1016/j.jnucmat.2020.152733.

[54] D.P. da Fonseca, A. Otsuka, M.V. dos S. Rezende, J.L.O. Santos, A.S. Souza, V. Altunal, Z. Yegingil, H. Lima, Structural, mechanical, dielectric and defect properties of Eu-doped BeO ceramics: a computational and experimental approach, Ceram. Int. 49 (18) (2023) 29647–29658, https://doi.org/10.1016/j.ceramint.2023.06.193.

[55] N. Sarigul, M. Surucu, B. Aydogan, Energy response factor of BeO dosemeter chips: a Monte Carlo simulation and general cavity theory study, Radiat. Protect. Dosim. 185 (3) (2019), https://doi.org/10.1093/rpd/ncz010.

[56] F. Spurný, R. Medioni, G. Portal, Energy transfer to some TLD materials by neutrons; comparison of theoretical and experimental data, Nucl. Instrum. Methods 138 (1) (1976) 165–171, https://doi.org/10.1016/0029-554X(76)90161-0.

[57] A. Seif, E. Zahedi, A DFT studies of structural and quadrupole coupling constants properties in C-doped BeO nanotubes, Superlattice. Microst. 50 (5) (2011) 539–548, https://doi.org/10.1016/j.spmi.2011.08.016.

[58] C.E. Tzeliou, M.A. Mermigki, D. Tzeli, Review on the QM/MM methodologies and their application to metalloproteins, Molecules 27 (9) (2022) 2660, https://doi.org/10.3390/molecules27092660.

[59] P. Hohenberg, W. Kohn, Inhomogeneous electron gas, Phys. Rev. 136 (B864) (1964), https://doi.org/10.1103/PhysRev.136.B864.

[60] W. Kohn, L.J. Sham, Self-consistent equations including exchange and correlation effects, Phys. Rev. 140 (1965) A1133–A1138, https://doi.org/10.1103/PhysRev.140.A1133.

[61] C.G. Van de Wallea, J. Neugebauer, First-principles calculations for defects and impurities: applications to III-nitrides, J. Appl. Phys. 95 (8) (2004) 15, https://doi.org/10.1063/1.1682673.

[62] R. Chen, G. Fogel, C.K. Lee, A new look at the models of the superlinear dose dependence of thermoluminescence, Radiat. Prot. Dosimetry 65 (1) (1996) 63–68, https://doi.org/10.1093/oxfordjournals.rpd.a031683.

[63] A.M. Sadek, G. Kitis, Impact of non-fulfillment of the super position principle on the analysis of thermoluminescence glow-curve, Radiat. Meas. 116 (2018) 14–23, https://doi.org/10.1016/j.radmeas.2018.06.016.

[64] P. Giannozzi, S. Baroni, N. Bonini, M. Calandra, R. Car, C. Cavazzoni, D. Ceresoli, G.L. Chiarotti, M. Cococcioni, I. Dabo, A. Dal Corso, S. de Gironcoli, S. Fabris, G. Fratesi, R. Gebauer, U. Gerstmann, C. Gougoussis, A. Kokalj, M. Lazzeri, L. Martin-Samos, N. Marzari, F. Mauri, R. Mazzarello, S. Paolini, A. Pasquarello, L. Paulatto, C. Sbraccia, S. Scandolo, G. Sclauzero, A.P. Seitsonen, A. Smogunov, P. Umari, R.M. Wentzcovitch, Quantum ESPRESSO: a modular and open-source software project for quantum simulations of materials, J. Phys. Condens. Matter 21 (2009) 395502, https://doi.org/10.1088/0953-8984/21/39/395502.

[65] J.P. Perdew, K. Burke, M. Ernzerhof, Generalized gradient approximation made simple, Phys. Rev. Lett. 77 (18) (1996) 3865, https://doi.org/10.1103/PhysRevLett.77.3865.

[66] W. Koch, M.C. Holthausen, A Chemist's Guide to Density Functional Theory, second ed., Wiley-VCH, 2001.

[67] A. Jain, S.P. Ong, G. Hautier, W. Chen, W.D. Richards, S. Dacek, S. Cholia, D. Gunter, D. Skinner, G. Ceder, K.A. Persson, The Materials Project: a materials genome approach to accelerating materials innovation, Apl. Mater. 1 (2013) 011002, https://doi.org/10.1063/1.4812323.

[68] A. Dal Corso, Pseudopotentials periodic table: from H to Pu, Comput. Mater. Sci. 95 (2014) 337–350, https://doi.org/10.1016/j.commatsci.2014.07.043.

[69] H. Schröder, J. Hühnert, T. Schwabe, Evaluation of DFT-D3 dispersion corrections for various structural benchmark sets, J. Chem. Phys. 146 (4) (2017) 044115, https://doi.org/10.1063/1.4974840.

[70] G. Kitis, J.M. Gomez-Ros, J.W.N. Tuyn, Thermoluminescence glow-curve deconvolution functions for first, second and general orders of kinetics, J. Phys. D Appl. Phys. 31 (19) (1998) 2636–2641, https://doi.org/10.1088/0022-3727/31/19/037.

[71] G. Kitis, N.D. Vlachos, General semi-analytical expressions for TL, OSL and other luminescence stimulation modes derived from the OTOR model using the Lambert W-function, Radiat. Meas. 48 (1) (2013) 47–54, https://doi.org/10.1016/j.radmeas.2012.09.006.

[72] E. Şahiner, Deconvolution analysis of thermoluminescent glow curves in various commercial dosimeters using two different approaches in the framework of the one-trap, one-recombination model, Turkish J. Phys. 41 (6) (2017) 477–490, https://doi.org/10.3906/fiz-1704-25.

[73] P. Konstantinidis, S. Kioumourtzoglou, G.S. Polymeris, G. Kitis, Stimulated luminescence; Analysis of complex signals and fitting of dose response curves using analytical expressions based on the Lambert W function implemented in a commercial spreadsheet, Appl. Radiat. Isot. 176 (July) (2021) 109870, https://doi.org/10.1016/j.apradiso.2021.109870.

[74] R. Chen, Glow curves with general order kinetics, J. Electrochem. Soc. 116 (9) (1969) 1254–1257, https://doi.org/10.1149/1.2412291. September.

[75] R. Chen, On the calculation of activation energies and frequency factors from glow curves, J. Appl. Phys. 40 (2) (1969) 570–585, https://doi.org/10.1063/1.1657437.

[76] G. Kitis, V. Pagonis, Peak shape methods for general order thermoluminescence glow-peaks: a reappraisal, Nucl. Instruments Methods Phys. Res. Sect. B Beam Interact. with Mater. 262 (2) (2007) 313–322, https://doi.org/10.1016/j.nimb.2007.05.027.

[77] G. Kitis, R. Chen, V. Pagonis, Thermoluminescence glow-peak shape methods based on mixed order Kinetics, Phys. Status Solidi Appl. Mater. Sci. 205 (5) (2008) 1181–1189, https://doi.org/10.1002/pssa.200723470.

[78] Y.S. Horowitz, D. Yossian, Computerised glow curve deconvolution: application to thermoluminescence dosimetry, Radiat. Prot. Dosimetry 60 (1) (1995) 1–114, https://doi.org/10.1093/oxfordjournals.rpd.a082702.

[79] Y. Chen, M.E. Turiansky, C.G. Van de Walle, First-principles study of quantum defect candidates in beryllium oxide, Phys. Rev. B 106 (2022) 174113, https://doi.org/10.1103/PhysRevB.106.174113.

[80] P.G. Konstantinidis, E. Tsoutsoumanos, G.S. Polymeris, G. Kitis, Discovering excited states; an innovative technique for the study of recombination pathways, Radiat. Phys. Chem. 212 (2023) 111112, https://doi.org/10.1016/j.radphyschem.2023.111112.

[81] M. Ozcan, V. Altunal, Z. Yegingil, Investigation of the electronic band gap tuning by Si doping on BeO using UV–VIS spectroscopy and density functional theory, Mater. Today Commun. 39 (2024) 109328, https://doi.org/10.1016/j.mtcomm.2024.109328.